

Voids in cosmological simulations over cosmic time

Radosław Wojtak^{1,2*}, Devon Powell¹, Tom Abel¹

¹*Kavli Institute for Particle Astrophysics and Cosmology, Stanford University, SLAC National Accelerator Laboratory, Menlo Park, CA 94025, USA*

²*Dark Cosmology Centre, Niels Bohr Institute, University of Copenhagen, Juliane Maries Vej 30, DK-2100 Copenhagen Ø, Denmark*

31 March 2016

ABSTRACT

We study evolution of voids in cosmological simulations using a new method for tracing voids over cosmic time. The method is based on tracking watershed basins (contiguous regions around density minima) of well developed voids at low redshift, on a regular grid of density field. It enables us to construct a robust and continuous mapping between voids at different redshifts, from initial conditions to the present time. We discuss how the new approach eliminates strong spurious effects of numerical origin when voids evolution is traced by matching voids between successive snapshots (by analogy to halo merger trees). We apply the new method to a cosmological simulation of a standard Λ CDM cosmological model and study evolution of basic properties of typical voids (with effective radii $6h^{-1}\text{Mpc} < R_v < 20h^{-1}\text{Mpc}$ at redshift $z = 0$) such as volumes, shapes, matter density distributions and relative alignments. The final voids at low redshifts appear to retain a significant part of the configuration acquired in initial conditions. Shapes of voids evolve in a collective way which barely modifies the overall distribution of the axial ratios. The evolution appears to have a weak impact on mutual alignments of voids implying that the present state is in large part set up by the primordial density field. We present evolution of dark matter density profiles computed on isodensity surfaces which comply with the actual shapes of voids. Unlike spherical density profiles, this approach enables us to demonstrate development of theoretically predicted bucket-like shape of the final density profiles indicating a wide flat core and a sharp transition to high-density void walls.

Key words: methods: numerical – dark matter – large-scale structure of Universe

1 INTRODUCTION

Cosmic voids are the most widespread and faintest structures in the Universe. They occupy around 80 percent of space containing only 15 per cent of the total mass (Falck & Neyrinck 2015; Cautun et al. 2014). Driven by current and upcoming massive cosmological surveys, a growing interest in voids enters a phase of studies aimed at exploring various prospects of using voids as a complementary means for probing the nature of dark energy (Lavaux & Wandelt 2012), dark matter (Hellwing & Juszkiewicz 2009; Yang et al. 2015) or gravity (Li et al. 2012; Cai et al. 2015) on large scales. Despite this promising potential of voids as cosmological probes, we lack a comprehensive understanding of their evolution and the origin of their properties.

The basic framework for understanding evolutionary processes of cosmic voids was introduced by Sheth & van de Weygaert (2004) on the basis of excursion set theory (see also the review of van de Weygaert & Platen 2011). Unlike dark matter haloes, voids can either grow over time or can be destroyed through the gravitational collapse of the boundary walls. Which evolutionary paths voids follow depends on void sizes and their position in the void hierarchy. Small distinct voids tend to collapse, whereas large voids undergo expansion. The expansion of voids render their interior similar to finite open universes with self-similar structures of their cosmic web (Gottlöber et al. 2003; Aragon-Calvo et al. 2010). The evolution of the hierarchical void network was studied in numerical simulations (van de Weygaert & van Kampen 1993), in the context of the adhesion approximation (Sahni et al. 1994) and excursion set theory (Sheth & van de Weygaert 2004). Most approaches focus on evolution

* E-mail: wojtak@stanford.edu

of various statistics of voids such as void abundances (Sutter et al. 2014a) or overall distributions of such properties as sizes or shapes (Bos et al. 2012). However, considering overall statistics may conceal many interesting aspects of evolution of individual voids. As we shall demonstrate in this work, tracing evolution of individual voids has potential to unveil more complex and richer reality of evolutionary processes than tracing evolution of an overall statistics of a void population as a whole.

Tracing the evolution of individual voids in cosmological simulations requires using a robust method for tracking these objects between snapshots. One can attempt to do this by applying standard algorithms for constructing merger trees of dark matter haloes. Voids are found at different moments of simulations by means of tracking IDs of particles found in their interiors. This approach was adopted by Sutter et al. (2014a) who used it to study formation, evolution and destruction of voids in cosmological simulations. Despite its straightforward implementation, the method is not expected to be accurate enough to separate genuine void evolution from a number of artificial effects related to the way of generating void catalogues and using particles as void tracer. In this work, we analyse performance of this approach and propose a new method which circumvents a number of recognized problems. The new method of tracking voids in simulations is built upon some generic properties of voids found with methods employing the watershed transform (Platen et al. 2007; Neyrinck 2008).

The current-state cosmic web was already present in the initial fluctuations of the primordial density field (Bond et al. 1996). Therefore, it is natural to think that the present voids can be mapped into underdense regions around initial troughs of the primordial density field (van de Weygaert & van Kampen 1993). Remarkable resemblance between initial and final cosmic web suggests that initial underdense regions should arrange most of the properties of well-developed voids such as shapes and relative alignments. On the other hand, one should also expect important effects from a late-time non-linear evolution driven by tidal forces and constraints resulting from evolution of adjacent voids (Platen et al. 2008). However, it is not clear to what degree these effects erase the initial arrangement of the void network and to what degree voids retain their initial properties. In our work, we address this nature-nurture problem for the first time in a fully quantitative way. Applying a newly developed method for tracking voids in cosmological simulations we study how non-linear evolution affects the properties of voids acquired from initial troughs in the primordial density field.

Voids are traditionally defined as parts of space with the mean density below a certain fixed limit. The most commonly adopted density limit is 20 per cent of the background density. The limit is derived in an analytic model of void evolution and signifies a moment of the first shell crossing leading to the formation of void boundaries (Sheth & van de Weygaert 2004). Despite a deep theoretical motivation, this approach narrows substantially the definition of voids. In particular, it automatically imposes the void formation time as the moment when void's density minimum crosses the assumed density threshold (Sutter et al. 2014a). However, the process of void formation should be rather regarded as continuous in the course of time. Recalling the fact that

the overall arrangement of the cosmic web is already present in the primordial density field, we should think of void formation as a gradual process increasing a density contrast between void cores and boundary walls. Following this picture we define voids as distinct underdense regions regardless of their evolutionary stage and thus regardless of their minimum or mean density. This simple definition allows us also to avoid a semantic ambiguity of possible terms which would have to be introduced in order to distinguish voids after formation time from void progenitors or protovoids before that time.

The paper is organized as follows. In Section 2 we describe all elements of the void finder: density estimator, the watershed algorithm and the method of generating void catalogues. In Section 3 we describe the new method of tracking voids in cosmological simulations and compare it to results from applying a direct implementation of a halo merger tree generator. We apply the new method to a standard cosmological simulation in Section 4, where we quantify evolution of various properties of individual voids (sizes, shapes, alignments and dark matter density distribution) from initial conditions to the present time. We conclude and summarize in Section 5.

2 VOID FINDER

Voids can be found in various ways (see e.g. Colberg et al. 2008). Many methods define voids as regions devoid of dark matter (Platen et al. 2007) or dark matter haloes (Gottlöber et al. 2003), other methods utilize kinematic or dynamical features such as divergence of velocity field (Hoffman et al. 2012) or tidal instability in smoothed density field (Hahn et al. 2007; Cautun et al. 2013). Some methods impose certain properties of voids such as shapes or density threshold, other techniques avoid fixing any of them and find voids in a non-parametric way. Void finders shall be also distinguished with respect to whether they can be applied to observational data or not. In general, void finders which need more sophisticated information than halo or galaxy distribution have more limited applicability to observations.

In our study we find voids as underdense regions in dark matter density field. Without attempting to show superiority of this approach over other methods, we emphasize that void finders based on this operational definition take a leading role in studying voids both in cosmological simulations and observations. Two most commonly used void finders, ZOBOV (ZOnes Bordering On Voidness; Neyrinck 2008) and its alteration VIDE (the Void Identification and Examination tool; Sutter et al. 2015), are arguably the most successful implementations (see also Way et al. 2015). Voids found as underdense regions appear to be visually appealing elements of the cosmic web. Some void finders such as ZOBOV can be run in a non-parametric way that is essential to avoid imposing some preconceptions on what voids should look like. The same void finders are also capable of unveiling hierarchical network of voids which is one of the most characteristic properties of these objects (see e.g. Aragon-Calvo et al. 2010; Aragon-Calvo & Szalay 2013).

We build our void finder by full analogy to ZOBOV. The only difference between our implementation and the original code is the way we compute the density field. Instead of a

Voronoi diagram employed in ZOBOV, we use a Lagrangian Tessellation Field Estimator on a regular grid (Abel et al. 2012). The two remaining parts of the void finder, i.e. the watershed transform (Platen et al. 2007) and a method of building physical voids, remain unchanged. We use regular density grid in order to optimize finding evolution of voids over successive snapshots of a simulation. Bearing in mind that voids retain their initial volumes rather than masses, it is natural to define voids as sets of pixels in space rather than a set of particles. In the latter case (for Voronoi tessellation), identification of voids in different snapshots becomes more ambiguous due to the fact that particles occupy void boundaries (walls) and therefore they are likely exchanged between adjacent voids. In the following subsections we describe all parts of our void finder in more detail.

2.1 Density estimator

We calculate the density field using the novel approach proposed by Abel et al. (2012) and Shandarin et al. (2012) alongside the exact conservative voxelization method of Powell & Abel (2015).

Density estimators for N -body data have traditionally relied on depositing point particles to a regular grid using cloud-in-cell, adaptive kernel smoothing, Voronoi tessellation, or some other such technique (see e.g. Hockney & Eastwood 1988, Neyrinck 2008). These are subject to sampling noise and most do not give a well-defined density field everywhere in space. This is especially true in regions of low particle density (voids), so we require a smoother and more physically faithful method.

The approach of Abel et al. (2012) and Shandarin et al. (2012) instead discretizes the dark matter mass into tetrahedra, where the particles are demoted to Lagrangian tracers that serve as vertices of these tetrahedral mass elements. In more technical terms, we model the cold dark matter fluid as a piecewise-linear approximation to a three-manifold embedded in the six-dimensional phase-space. This approach gives a density field that is well-defined everywhere in configuration space, in contrast with a set of point particles as in the traditional N -body case. So far, it has been applied successfully to gravitational lensing (Angulo et al. 2014), large-scale structure (Hahn et al. 2015), simulations (Hahn et al. 2013; Hahn & Angulo 2016; Sousbie & Colombi 2015), and visualization (Kaehler et al. 2012).

We apply a piecewise-linear density interpolation across each tetrahedron. This gives the smoothest density maps and has proven the most effective at revealing voids through the watershed transform. The density at each tracer vertex v is given by a volume-weighted average of the masses of the tetrahedra sharing that vertex, $t \in v$:

$$\rho_v = \frac{\sum_{t \in v} m_t}{\sum_{t \in v} V_t}.$$

This gives a density map that is smooth and continuous.

Given this discretization of the dark matter into a set of tetrahedra with linearly-varying density, we require a way of depositing this density field on to a uniform Cartesian grid on which to calculate the watershed transform. We do this using the conservative voxelization method of Powell & Abel (2015), which robustly calculates the exact volume

and moments of intersection between each tetrahedral element and each cubical cell in the target grid, then computes the amount of mass to be transferred. This guarantees that mass is globally and locally conserved and that the resulting density field is smooth and naturally anti-aliased.

The final result is a density field on a Cartesian grid that is smooth and well-defined everywhere, especially in voids where a particle sampling method would be insufficient.

2.2 Watershed transform

The watershed transform divides space into contiguous zones, the so-called watershed basins. Every watershed basin contains a local density minimum and it is delineated by a surface which is a 3D analogue of a ridge line in a 2D density field (for a more detailed description see Platen et al. 2007). Watershed basins are typically much smaller than physical voids; therefore, the final step of the void finder involves merging basins into voids. Following the algorithm implemented in ZOBOV, we build voids by merging all adjacent watershed basins which are shallower than the initial one. Basins are merged according to the order of saddle points at the boundaries between them. The process of merging stops when it encounters a basin with a minimum density lower than the minimum density of the initial basin (for more details see Neyrinck 2008).

The way the adopted method builds voids is fully determined by orders of density minima and saddle points of the density field. The total volume of all voids exceeds the total volume of watershed basins (volume of the simulation box). This means that voids overlap in space and form a hierarchical network such that every void is a subvoid of only one void and it may contain an unlimited number of subvoids (see e.g. Lavaux & Wandelt 2012). The network consists of many levels of hierarchical relations between voids. Hereafter we refer to a void-subvoid sequence as, respectively, the top and bottom levels of the void hierarchy.

We perform watershed transform and build voids using the *jozov* module of ZOBOV. Despite the fact that the ZOBOV computes density using Voronoi tessellation, the *jozov* module can easily operate on different density grids. This only requires appropriate labelling pixels and specifying connectivity between them. We assume that every pixel of a regular cubical grid has 26 adjacent pixels sharing its faces or vertices.

In most applications, void finders invoke density thresholds which define the lowest density on the boundary surface between every two adjacent voids (ZOBOV) or impose a limit on density in void cores. Since our main goal is to trace evolution of voids from initial conditions to the present time, our void finder cannot rely on any density threshold. We therefore do not assume any density limits on void cores and void barriers and find voids in a fully non-parametric way. This approach is feasible in our case because the adopted density grid smoothens the density on scales comparable to dark matter haloes and thus it automatically eliminates the possibility of spurious detections in high density regions (Neyrinck 2008). It also brings back the original idea of ZOBOV devised as a non-parametric void finder.

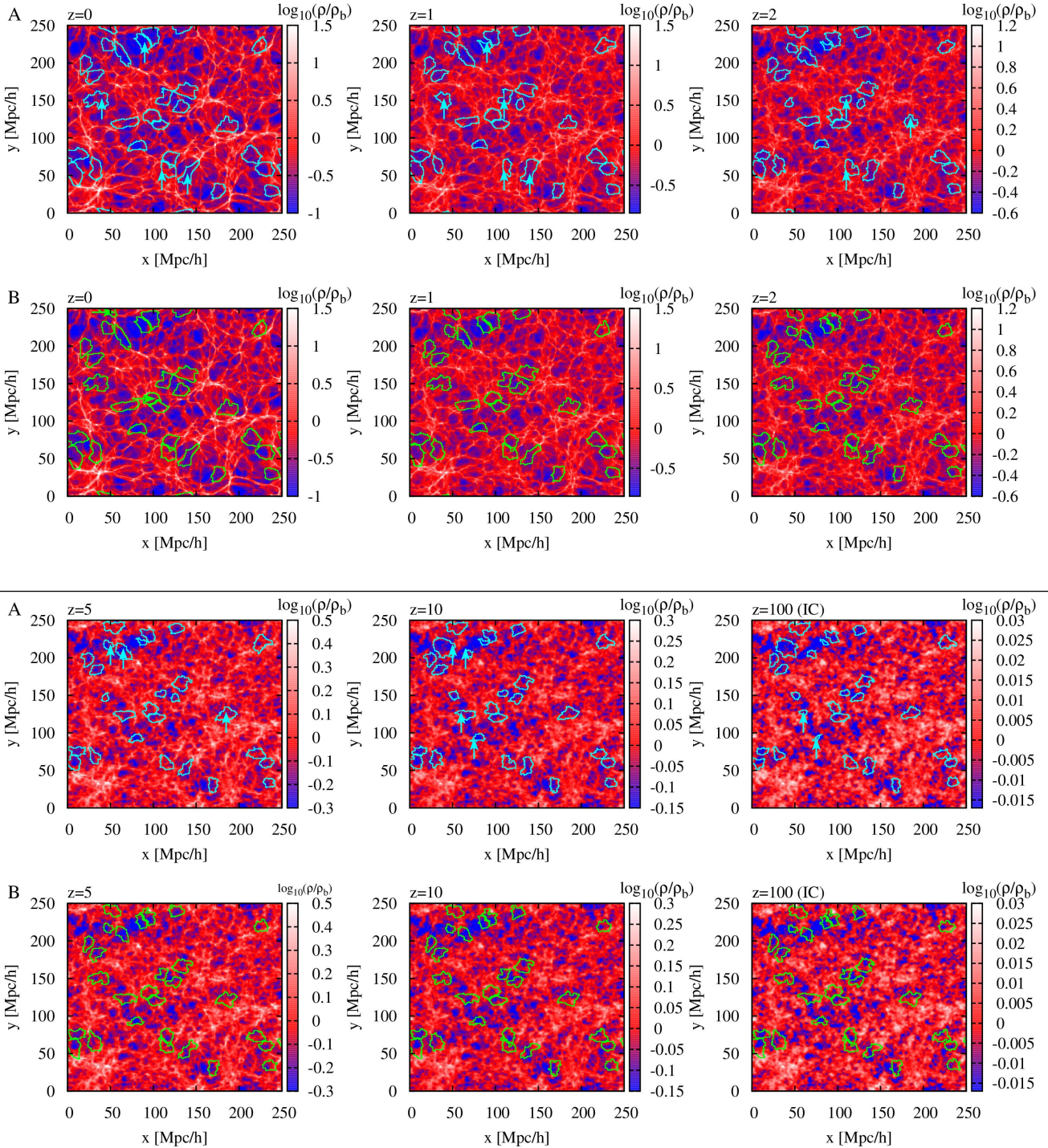


Figure 1. Two methods of tracking voids in cosmological simulations. The upper row (A) shows evolution of voids found by matching voids between adjacent snapshots (with watershed basins merged into voids in every snapshot independently). The bottom row (B) shows evolution of voids found by means of tracking watershed basins back in time under the assumption that voids consist of the same groups of basins at all times (with watershed basins merged into voids only once at $z = 0$). Both methods start with the same group of voids at $z = 0$ (upper left panels) and track them back in time to initial conditions. Every panel shows voids boundaries projected on to the image plane and log of the density field inside a $10h^{-1}$ Mpc thick slab. Voids at $z = 0$ (upper left panels) have effective radii between $8h^{-1}$ Mpc and $10h^{-1}$ Mpc and lie no further than 30 per cent of their effective radii from the image plane. Results of void tracking are presented in the consecutive panels corresponding to snapshots at redshifts $z = 1, 2, 5, 10, 100$ (initial conditions). Tracking watershed basins (row B) yields evolutionary tracks of voids which are continuous at all times (voids coevolve with their boundaries). On the other hand, matching voids between adjacent snapshots (row A) gives rise to spurious reconfigurations resulting from reordering of density minima and saddle points, in large part due to unresolved small-scale modes and numerical rounding. Voids undergoing most visible reconfigurations are indicated with arrows (two snapshots before and after the event).

2.3 Cosmological simulation

For the purpose of our studies we ran a low resolution N -body simulation of dark matter structure formation in a Λ CDM cosmological model with Planck cosmological parameters, i.e. $\Omega_m = 0.31$, $\Omega_\Lambda = 0.69$, $\sigma_8 = 0.82$ and $h = 0.67$ (Planck Collaboration et al. 2014). The initial conditions were generated using the Multi-Scale Initial Conditions code (MUSIC; Hahn & Abel 2011) with the transfer function given by a fitting formula obtained by Eisenstein & Hu (1998). The simulation box has a side length equal to $250h^{-1}\text{Mpc}$ and contains $N_p = 256^3$ particles. The adopted mass resolution allows us to resolve voids with effective radii larger than $\sim 5h^{-1}\text{Mpc}$.

The simulation was run using the Gadget-2 N -body code (Springel 2005) and snapshots used for tracing void evolution were saved with a temporal resolution of $\Delta a/a = 0.05$. The density field used for finding voids in all snapshots was computed on a regular grid with $N_g = 256^3$ cells corresponding to a grid spacing of nearly $1h^{-1}\text{Mpc}$. The adopted grid size smoothens the density field on scales comparable to largest dark matter haloes.

3 VOID TRACKING

Evolution of voids is distinct from evolution of dark matter haloes in many respects. Many evolutionary processes do not have their counterparts in mechanisms of halo formation. Well known examples of such processes are disappearance of voids caused by collapse of walls around them or void merging due to dilution of boundaries between them. The comprehensive description of all these processes as well as theoretical framework based on the excursion set theory was outlined by Sheth & van de Weygaert (2004). In our work we shall address just one aspect of this complexity of voids evolution, namely evolution of various properties of voids between initial conditions and redshift $z = 0$. A practical problem arising here is a robust method for tracking voids in cosmological simulations.

3.1 Simple void matching

Voids can be tracked in simulations in a similar way as dark matter haloes. A common tool devised for this purpose is a merger tree. In the context of dark matter haloes, merger trees represent physical processes of halo formation and tracking dark matter haloes is reduced to finding the main progenitors. From a more abstract point of view, merger tree is merely a means of linking or associating objects detected at different snapshots. It is therefore tempting to think that the same algorithms used for building halo merger trees can be utilized to track cosmic voids by finding a sequence of void progenitors. This approach was already presented by Sutter et al. (2014a). Their method employed the VELOCIRAPTOR tree builder code, a publicly available code for generating halo merger trees, which was directly applied to catalogues of voids found in a cosmological simulation. This direct implementation of the halo merger tree code was feasible thanks to the fact that voids were found on a Voronoi grid and therefore they were defined by IDs of particles. On the one hand, one can appreciate that the same merger tree

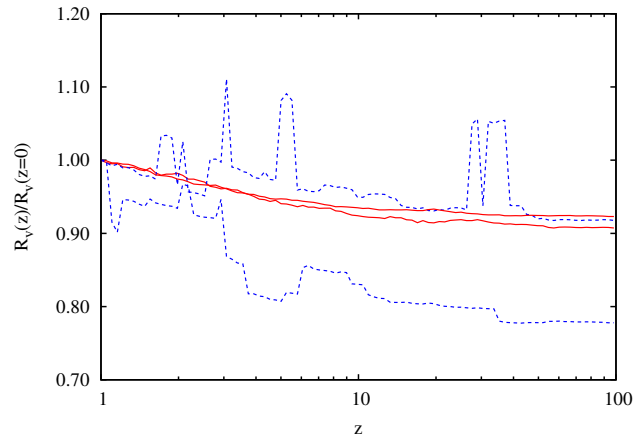


Figure 2. Redshift evolution of effective radii of two typical voids selected from $z = 0$ snapshot shown in Fig. 1 (indicated by arrows on $z = 0$ panel in row B). The solid red lines show results from tracking watershed basins of $z = 0$ voids back in time (illustrated by panels B in Fig. 1) and the blue dashed lines from matching voids between successive pairs of adjacent snapshots (illustrated by panels A in Fig. 1). The former method yields a continuous evolution of void boundaries over time resulting in smooth redshift profiles. The latter method generates spurious and instantaneous reconfigurations, well visible as strong discontinuities of the profiles.

code can be applied both to haloes and voids. On the other hand, one can notice the following caveat of this approach. As pointed out by Sutter et al. (2014a), identifying voids by particles is subject to some degree of ambiguity. Most particles occupy boundaries of voids and therefore they are often exchanged between adjacent voids. This makes identification of voids in different snapshots less accurate. The process of matching voids between different snapshots can be substantially improved if voids were defined in terms of comoving volume they occupy (IDs of pixels of a regular grid in comoving space) rather than mass they contain (IDs of particles). This can be automatically achieved by running a void finder on density fields computed on a regular grid adopted in our density estimator.

We use our void finder described in section 2 to detect voids in all snapshots of the simulation. Voids are specified as contiguous groups of pixels. We track every individual void by creating a sequence of the best matching voids between successive pairs of adjacent snapshots. The best matching void is found by maximizing degree of overlap in space which is quantified by $n_{AB}^2/(n_A n_B)$, where n_{AB} is the number of pixels shared by void from snapshot A and void from snapshot B , n_A and n_B are the numbers of pixels in the two voids.

The upper panels (A) in Fig. 1 show an example of tracking a group of voids from redshift $z = 0$ to initial conditions. The contours show projections of voids on to the image plane and the map shows log of the density integrated inside a slab of a $10h^{-1}\text{Mpc}$ thickness. In order to maximize correspondence between the density map and voids we select voids which lie no further than 30 per cent of their effective radii from the image plane at $z = 0$, where the effective void radius R_v is radius of a sphere enclosing volume V equal to the void's volume, i.e.

$$R_v = \left(\frac{3V}{4\pi} \right)^{1/3}. \quad (1)$$

All voids shown in Fig. 1 have effective radii in a range between $8h^{-1}\text{Mpc}$ and $10h^{-1}\text{Mpc}$ at $z = 0$, well above the resolution limit.

Fig. 1 illustrates that the method of matching voids between adjacent snapshots yields in principle a reasonable mapping between void boundaries at different redshifts. Some voids clearly coevolve with the cosmic web and remain delineated by the same boundary walls at all redshifts. However, a closer inspection of the plot reveals a group of voids which undergo instantaneous reconfigurations such as loss of volume or incorporation of some parts of adjacent voids (see voids indicated by arrows). These processes result merely from reordering of density minima and saddle points which determine a way how watershed basins are merged into voids. Therefore, they are related to the adopted definition of voids rather than genuine evolution of voids. The problem becomes even more complicated if we realize that reordering of critical points in the density field is caused in some part by unresolved small-scale modes and thus it is a stochastic process. Another important factor is numerical rounding.

We assess the impact of numerical resolution on the apparent reconfigurations of voids by comparing voids found in two simulation runs with the same initial conditions but different mass resolutions. For this purpose we reran our main simulation with $N_p = 512^3$ particles, computed the density field using data downsampled to $N_p = 256^3$ and then found voids in the same way as described in section 2. Matching voids between the catalogues from high and low resolution runs we find that typical degree of matching is much smaller than for a naive one-to-one correspondence between both void catalogues. The mean space overlap $n_{AB}^2/(n_{ANB})$ between best matched voids with effective radii between $6h^{-1}\text{Mpc}$ and $20h^{-1}\text{Mpc}$ is around 0.8 (up to 20 per cent relative difference in volume).

Fig. 2 illustrates more explicitly a stochastic nature of instantaneous reconfigurations of voids tracked by means of matching voids between successive pairs of adjacent snapshots. The dashed lines show the redshift evolution of effective radii of two representative voids from Fig. 1 indicated by arrows on $z = 0$ panel in row B. The redshift profiles clearly demonstrate that the reconfigurations occur in a random manner. In extreme cases, voids undergo a substantial change of their volumes and then return to their initial boundaries in the following snapshot. We conclude that a robust method for tracing evolution of voids and their properties should be capable of eliminating this purely numerical effect.

3.2 Tracking watershed basins

Spurious reconfigurations of voids demonstrated in the previous section result in large part from random reordering of the density minima and saddle points, caused by unresolved small-scale modes and numerical rounding. A simple way to circumvent this problem is to avoid merging watershed basins into voids at every snapshot independently. Instead, we propose to generate a void catalogue only once and then to track watershed basins back in time in order to find the

corresponding voids at different redshifts. We therefore assume that voids consist of the same groups of watershed basins at all times. We expect that this assumption guarantees a continuous mapping between void interiors or boundaries over time. On the other hand, one disadvantage of this approach is the fact that it is not expected to tackle such processes as void destructions, which changes the number of voids over time, and voids mergers, which are associated with physical reconfigurations in void network. The former processes can be captured by finding voids at high redshift and tracking them forward in time.

We track watershed basins of voids from $z = 0$ snapshot in a similar way as voids in the previous section. First we apply watershed transform to all snapshots. Then we match basins between every two adjacent snapshots in such a way that every basin contains the minimum of its best matching basin from the other snapshot. Watershed basins may not evolve in a continuous way. They can merge (more common) or split (less common) in the course of their evolution. Both processes are easily tracked as bifurcations in the linking relations between basins. For example, merging process occurs when at least two adjacent basins are lined to only one basin in a later time snapshot.

The bottom panels (B) in Fig. 1 show evolution of voids found by tracking watershed basins back in time. For the sake of objective comparison with the previous method (see the corresponding panels in the upper row, A), we use the same group of voids selected from $z = 0$ snapshot. Fig. 1 clearly demonstrates how differences between voids found by the two methods gradually increase at high redshifts. Whereas many voids from the method based on matching voids between snapshots (panels B) undergo unphysical reconfigurations (instantaneous loss of volume or incorporation of adjacent space), voids found by tracking watershed basins (panels A) are consistently delineated by the same boundaries at all redshifts. Closer examination of how the contours evolve between the panels shows that the method based on tracking watershed basins allows us to create a continuous mapping between voids interiors or boundaries at different redshifts.

Instantaneous reconfigurations in void tracking by means of matching voids between adjacent snapshots occur quite often. 50 per cent of voids change their volumes between adjacent snapshots by more than 50 per cent and nearly 70 per cent of them by more than 30 per cent. Reconfigurations may happen more than once and are more frequent at low redshifts. The corresponding fractions of voids undergoing comparable volume evolution are negligible ($\sim 10^{-3}$) when voids are tracked using the new method. This is illustrated by Fig. 2 which compares redshift evolution of effective radii of two representative voids selected from $z = 0$ panel in Fig. 1 (voids indicated with arrows on $z = 0$ panel in row A) and tracked back in time using the new method (solid red lines) or the previous method based on matching voids between adjacent snapshots (dashed blue lines). It is clear that the method based on tracking watershed basins eliminates spurious effects of the previous one and yields continuous redshift profiles.

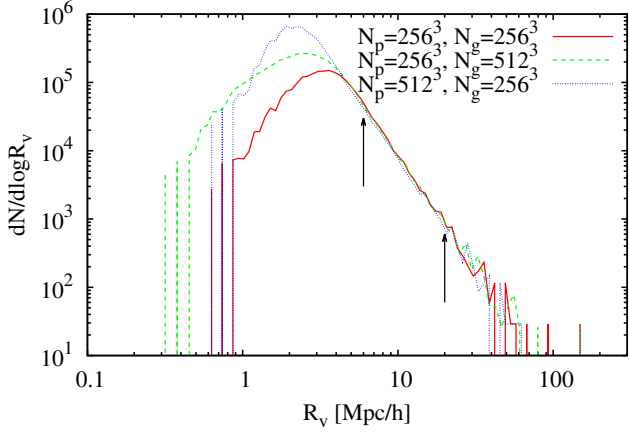


Figure 3. Distribution of void effective radii at redshift $z = 0$ in simulations with three different mass or grid resolutions given by the number of particles, N_p^3 , and cells of the density grid, N_g^3 , used for void finding. The black arrows show the range of void sizes adopted in this study. The selected voids have sizes well above the resolution limit.

4 EVOLUTION OF VOIDS

Here we use our new algorithm for tracking voids in cosmological simulations to study evolution of their basic properties. Since our main focus is to compare mature voids to their early state in initial conditions, it is natural to create a void catalogue at redshift $z = 0$ and then to find the corresponding voids in all remaining snapshots at higher redshifts. For practical reasons, we restrict our study to around 6100 voids with effective radii selected from a narrow range between $6h^{-1}\text{Mpc}$ and $20h^{-1}\text{Mpc}$ at $z = 0$. We therefore neglect a class of voids which might have collapsed before that redshift (Sheth & van de Weygaert 2004) and all results presented in this section show evolution of merely voids existing at redshift $z = 0$.

The selected voids have sizes comparable to typical sizes of voids found in observations (Paz et al. 2013). They are also well above the resolution limit of our primary simulation with $N_p = 256^3$ particles and $N_g = 256^3$ cells of the density grid used for finding voids. This is illustrated by Fig. 3 which shows the distribution of void effective radii in simulations with an increased mass or density grid resolution. For the adopted density grid resolution, voids contain from 10^3 to 4×10^4 pixels, arguably sufficient for a robust computation of all void properties considered in this work. For the sake of a sanity check, in a few instances we plot results from an analysis based on an increased grid resolution with $N_g = 512^3$ cells in order to demonstrate numerical convergence.

Fig. 4 illustrates variety of processes transforming initial voids into well developed voids at redshift $z = 0$. In this figure, we compare projected boundaries of voids from Fig. 1 at redshift $z = 0$ (filled contours) and to the corresponding boundaries in initial conditions (black contours). The main agent distorting shapes of voids and changing their orientations are tidal forces. Depending on how uniform the gravitational acceleration is across the void interiors, some voids gain bulk velocities and move in space. Many voids undergo expansion driven by a super-Hubble flow of their

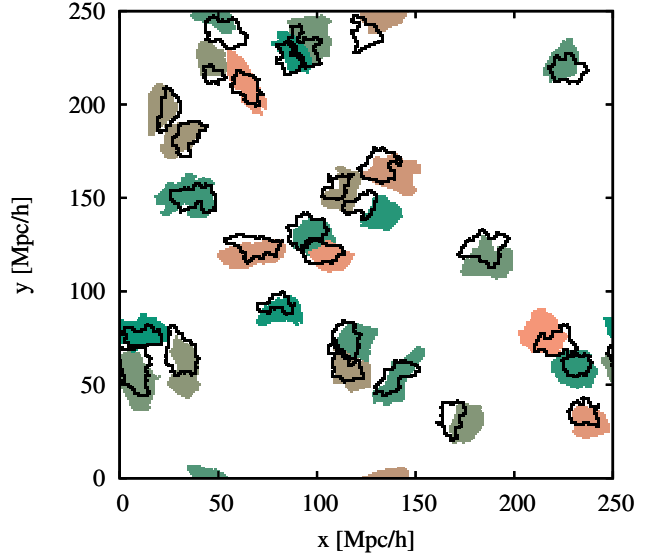


Figure 4. Projected boundaries of voids from Fig. 1 at redshift $z = 0$ (filled contours) and in initial conditions at $z = 100$ (maximally overlapping black contours). Voids at different redshifts are found by tracking watershed basins of $z = 0$ back in time. The picture illustrates a variety of evolutionary processes: bulk motion, anisotropic expansion or contraction leading to evolution of shapes and orientation of principle axes.

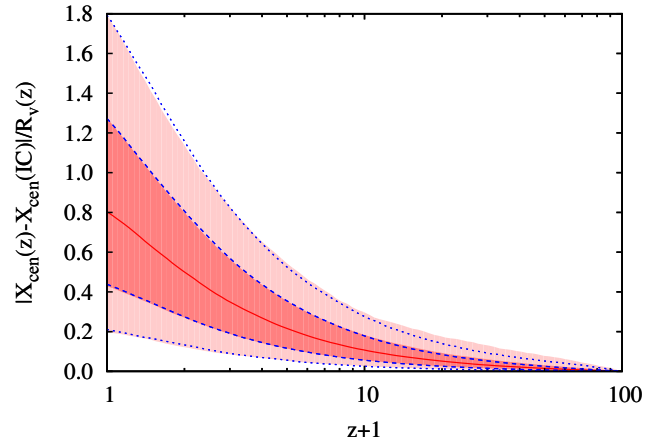


Figure 5. Displacement of geometric centres of voids between initial conditions ($z = 100$) and redshift z . Voids are traced in the simulation by means of tracking watershed basins of $z = 0$ voids back in time. The shaded contours show the 1σ and 2σ ranges of the distribution and the solid red line is the median profile. The selected voids have effective radii $6h^{-1}\text{Mpc} < R_v < 20h^{-1}\text{Mpc}$ at $z = 0$. The geometric centres move due to bulk motions of voids and anisotropic deformations of their boundaries. The dashed and dotted lines show the 1σ and 2σ ranges from an analysis based on an increased density grid resolution with $N_g = 512^3$ cells.

host voids (compare with the density field in Fig. 1). Finally, although not displayed in Fig. 4, it is important to note that all voids evacuate matter from their cores to their boundaries decreasing densities in their central parts from $\sim \rho_b$ in initial conditions to $\lesssim 0.2\rho_b$ at redshift $z = 0$.

As already illustrated in Fig. 4, voids undergo substan-

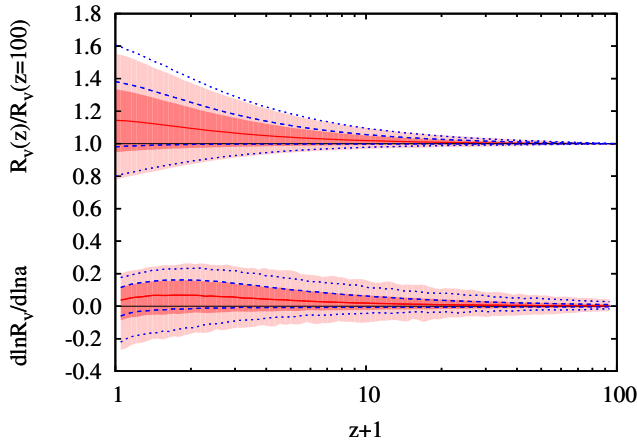


Figure 6. Redshift evolution of void effective radii and their logarithmic growth. Voids are traced in the simulation by means of tracking watershed basins of $z = 0$ voids back in time. The shaded contours show the 1σ and 2σ ranges of the distribution and the solid red line is the median profile. The selected voids have effective radii $6h^{-1}\text{Mpc} < R_v < 20h^{-1}\text{Mpc}$ at $z = 0$. The dashed and dotted lines show the 1σ and 2σ ranges from an analysis based on an increased density grid resolution with $N_g = 512^3$ cells.

tial modifications of their initial boundaries. Fig. 5 demonstrates spatial scales of this process in a more quantitative way. The shaded contours show the distribution of distances travelled by geometric centres X_{cen} (average position of all void pixels) between their initial positions in voids at $z = 100$ and positions in consecutive snapshots of the simulation. We checked that these displacements remain virtually the same when pixels are weighted by inverse density. This shows that the measured displacements of void geometric centres reflect genuine evolution of void interiors: bulk motions (Lambas et al. 2016) and anisotropic deformations by tidal forces. As naturally expected for a linear evolution, geometric centres of voids at high redshifts remain at rest. The bulk growth of distances travelled by geometric centres of voids occur at low redshifts. Typical displacements reach 80 per cent of the final effective radii signifying that spatial scales of void evolution are comparable to their sizes. This in turn reflects a basic fact that typical sizes of void deformations are comparable to typical distances travelled by particles in cold dark matter cosmological model.

4.1 Void sizes

Fig. 6 shows effective radii of voids as a function of redshift. Most voids undergo slow expansion increasing their effective radii typically by 15 per cent. The process of expansion is characteristic for voids embedded in larger underdense regions which accelerate local expansion rate with respect to the global Hubble flow (super-Hubble flow). The opposite process may occur if walls around voids are sufficiently massive to initiate collapse and thus contraction of the voids interiors. Nearly 20 per cent of voids selected at redshift $z = 0$ undergo this process. The asymmetry between the number of contracting and expanding voids reflects asymmetry between overdense and underdense regions developed in a phase of non-linear evolution. Underdense regions fill

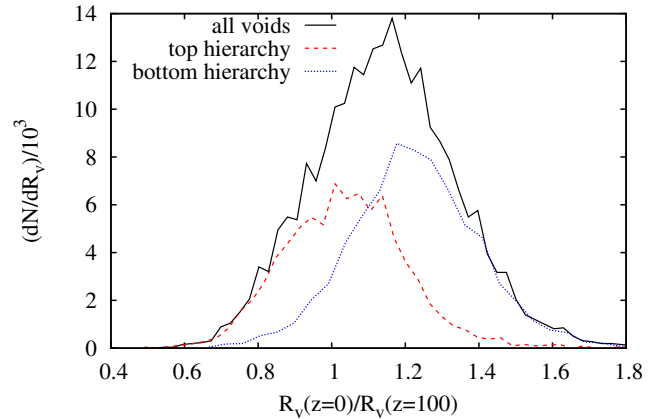


Figure 7. Distribution of growths of void sizes from $z = 100$ (initial conditions) to $z = 0$. The dashed (red) and dotted (blue) lines show the distributions for voids from the two topmost levels of the void hierarchy and from the remaining lower levels (subvoids). The dynamics of voids reflects their positions in the void hierarchy: the most expanding voids (the upper tail in the overall distribution) lie at the bottom of the hierarchy and the most collapsing ones (the lower tail in the overall distribution) lie at the top of the hierarchy. The selected voids have effective radii $6h^{-1}\text{Mpc} < R_v < 20h^{-1}\text{Mpc}$ at $z = 0$.

more space and therefore a void-in-underdensity configuration is more likely than void-in-overdensity.

Evolution of void sizes appear to be much less prominent than displacements of geometric centres shown in Fig. 5. Whereas there is a high probability that void retains its initial volume, its geometric centre is displaced by at least 20 per cent of the final effective radius. We therefore expect that evolution of void boundaries is much more complex than volumes they enclose. In fact, it is easy to imagine a number of processes changing shape or roughness of the boundary surface and preserving the enclosed volume.

The shaded contours in the bottom part of Fig. 6 show the distribution of the logarithmic growth of effective radii as a function of redshift. The growth at redshift $z(a)$ is estimated as

$$\frac{d \ln R_v}{d \ln a} = \frac{\ln[R_v(a + \delta a)/R_v(a)]}{\ln[(a + \delta a)/a]} \quad (2)$$

and averaged over two adjacent snapshots, i.e. $\delta a = \pm \Delta a$. Our results point to a much slower growth than what was obtained in recent studies by Sutter et al. (2014a). Typical logarithmic growth of void effective radii in our work is around 0.1 with a maximum at $z \approx 1$. We note that this estimate would substantially increase if the effect of spurious reconfigurations discussed in section 3 was not corrected.

The physical reason whether voids expand or contract is directly related to how much mass is retained in void boundaries. If the mass overdensity deposited in void boundary exceeds the mass underdensity in void, then walls around the void start to collapse and thus void itself starts to contract. Coincidentally, mass deposited in void boundary determines also its location in the void hierarchy: voids delineated by massive walls are more likely at the top levels of the hierarchy, whereas voids delineated by weak walls are more likely subvoids of larger voids (bottom of the hierarchy). We can

therefore expect that void dynamics reflects its position in the void hierarchy. Fig. 7 confirms this supposition. The figure shows the distributions of the growth of void sizes in different groups of voids split according to their positions in the void hierarchy: a half of voids at the top-most or bottom-most levels of the hierarchy. It is evident that all most contracting voids lie at the top of the hierarchy, while all most expanding voids belong to the bottom levels of the hierarchy (subvoids). This connection holds if we narrow the range of effective radii to $6h^{-1}\text{Mpc} < R_v < 8h^{-1}\text{Mpc}$. This indicates that the primary relationship between expansion rate of voids and their sizes (large voids tend to expand and small voids tend to collapse; see e.g. Hamaus et al. (2014); Sutter et al. (2014a)) is additionally modulated by their positions in void hierarchy.

4.2 Shapes

Fig. 4 shows evidently that shapes of voids evolve in time. Here we provide a more quantitative description of this process. In order to quantify shapes of voids, we compute the shape tensor S given by

$$S_{ij} = \sum_{k=1}^n [e_i \cdot (r_k - X_{\text{cen}})][e_j \cdot (r_k - X_{\text{cen}})], \quad (3)$$

where n is the number of pixels in void, r_k is the position vector of k -th pixel, X_{cen} is the position vector of void geometric centre (average position of all void pixels) and e_i with $i = 1, 2, 3$ are unit vectors oriented along x , y and z axis of the simulation box. Diagonalizing the shape tensor we obtain its eigenvalues: $s_a, s_b < s_a$ and $s_c < s_b$, which are proportional to squares of the principle axes of an ellipsoid approximating void shape. We measure void shapes in terms of axial ratios of the shape ellipsoids, i.e. major-to-minor axis ratio $a/c = \sqrt{s_a/s_c}$ and medium-to-minor axis ratio $b/c = \sqrt{s_b/s_c}$.

Fig. 8 shows axial ratios a/c (top panel) and b/c (bottom panel) of voids as a function of redshift. The upper contours on every panel show the overall distributions of axial ratios, while the lower contours show the distributions of a relative change in axial ratios of all individual voids, between redshift z and initial conditions. Comparing our results with those available in the literature (for $z = 0$ only), we find remarkable agreement regardless of differences in the adopted definitions of voids (see e.g. Platen et al. 2008; Shandarin et al. 2006).

As expected from the linear perturbation theory, voids at high redshift do not evolve their boundaries and thus retain their shapes. The bulk change of the shapes occurs at later time when every individual void can increase or decrease its axial ratio by up to ~ 0.2 , which is comparable to intrinsic scatter in the overall distributions. For the most typical evolutionary paths of voids, the b/c axial ratio does not change and the c/a axis ratio marginally decreases.

It is quite surprising to notice that a strong evolution of individual voids barely affects the overall distributions of axial ratios. One could expect that evolution of individual voids would at least broaden the distributions of axial ratios. However, what is clearly readable from Fig. 8 is that the distribution of b/c axis ratios remains the same at all redshifts, whereas the a/c distribution exhibits only a small

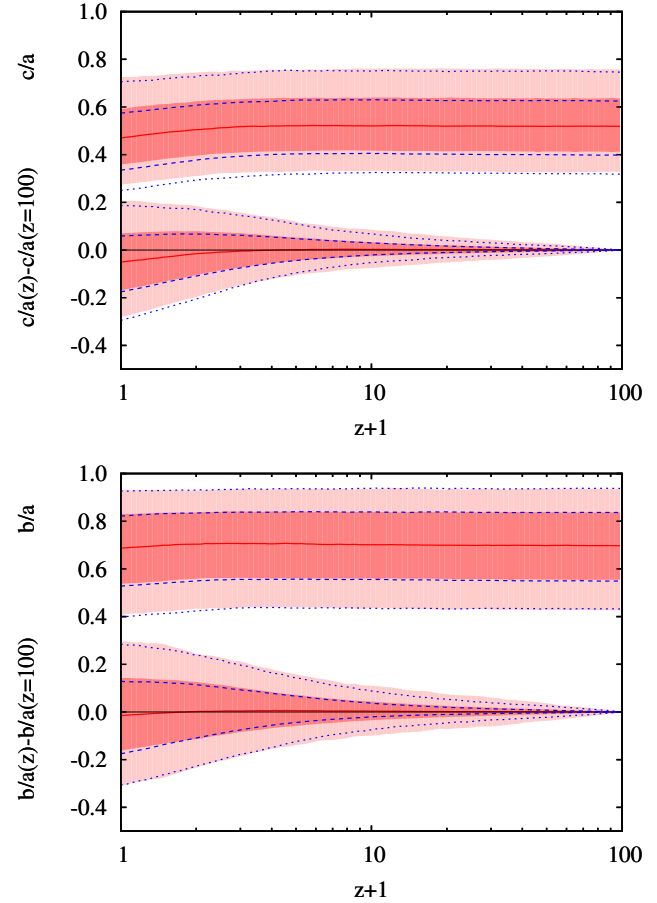


Figure 8. Shapes of voids as a function of redshift (top panel: major-to-minor axis ratio of the shape ellipsoids, c/a ; bottom panel: medium-to-minor axis ratio of the shape ellipsoids, b/c). The shaded contours show the 1σ and 2σ ranges of the distribution at every redshift. The top contours in both panels show the overall distributions of axial ratios and the lower ones demonstrate evolution of shapes of individual voids relative to the initial shapes at $z = 100$ (initial conditions). Individual voids change substantially their shapes; however, the overall distribution of axial ratios remains nearly the same. The dashed and dotted lines show the 1σ and 2σ ranges from an analysis based on an increased density grid resolution with $N_g = 512^3$ cells.

shift towards smaller values. The reason why the overall distributions of axial ratios do not evolve over time is related to phenomenon of collective evolution of voids. It is explained in Fig. 9 which shows the total change in b/c axial ratio as a function of their initial values calculated for voids found in initial conditions. The figure demonstrates that the most and the least elongated initial voids tend to evolve in two opposite directions on b/c axis: most elongated become less elongated in the course of evolution and least elongated become more elongated (see the black arrows indicating direction of the evolution). This effectively suppresses both tails of the shape distribution over time. However, loss in the tails of the distribution is simultaneously compensated by evolution of voids with initial shapes around the mean. These voids have equal chances of becoming more elongated or less elongated (see the black arrows). It appears that processes

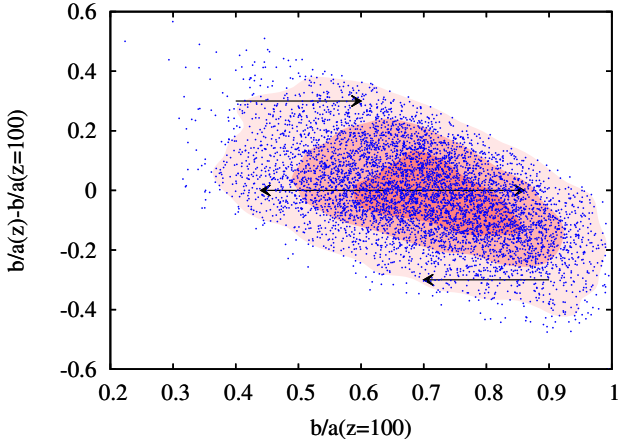


Figure 9. Evolution of void medium-to-minor axis ratios from $z = 100$ (initial conditions) to $z = 0$. The arrows show typical directions of the shape evolution in different parts of the initial shape distribution: most elongated ($b/a \lesssim 0.5$) and most spherical ($b/a \gtrsim 0.8$) voids evolve towards an average shape ($b/a \approx 0.65$), whereas voids with shapes around the average have equal chances of becoming more elongated or more spherical compensating loss in the tail of the shape distribution. This collective evolution of voids prevents the overall shape distribution from undergoing noticeable changes over time (see Fig. 8).

of suppression and compensation are so well tuned that the overall distribution of shapes does not evolve over time.

Considering an idealized model describing evolution of an isolated and aspherical void one can show that void should become gradually more spherical in the course of its evolution (Icke 1984). As pointed out by Shandarin et al. (2006), this reasoning is based on a major oversimplification. Voids do not evolve as isolated objects, but as a network of interconnected objects in which evolution of every individual void is constrained by evolution of its adjacent voids. The collective evolution of voids prevents them from gaining more spherical shapes. Our results reinforce this argument. As shown in Fig. 8, individual voids change their shapes with no global tendency towards sphericity. The mean axial ratio a/c becomes actually slightly smaller indicating evolution towards more elongated shapes. As far as evolution of individual voids, our results show that a randomly selected void in initial conditions has equal chances of becoming more elongated or more spherical.

Our results demonstrate that non-linear evolution has a strong impact on shapes of individual voids. This should be regarded as a caveat for any attempt to model the distribution of void shapes using linear perturbation theory applied to the Gaussian random density field (see e.g. Lee et al. 2005).

4.3 Alignment

Orientations of voids at redshift $z = 0$ are strongly correlated at separations up to $20h^{-1}\text{Mpc}$ (Platen et al. 2008). This kind of alignment is expected for all structures formed around peaks (or troughs for voids) of the Gaussian random density field (Desjacques & Smith 2008). Here we study to what degree the present alignment of voids is arranged in

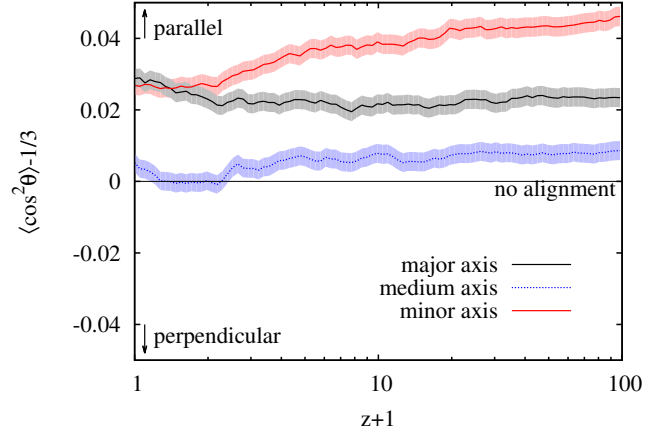


Figure 10. Alignment of voids as a function of redshift. The alignment is measured by the angle θ between the corresponding principle axes of voids separated by no more than $15h^{-1}\text{Mpc}$ (and excluding void-subvoid pairs). Positive or negative measure of the alignment shown on y-axis correspond to preferentially parallel or perpendicular orientations. The shaded bands show the 1σ errors from bootstrapping. Voids tend to be aligned in major and minor axes. This alignment is in large part arranged in the Gaussian primordial density field and only weakly modified in late-time evolution.

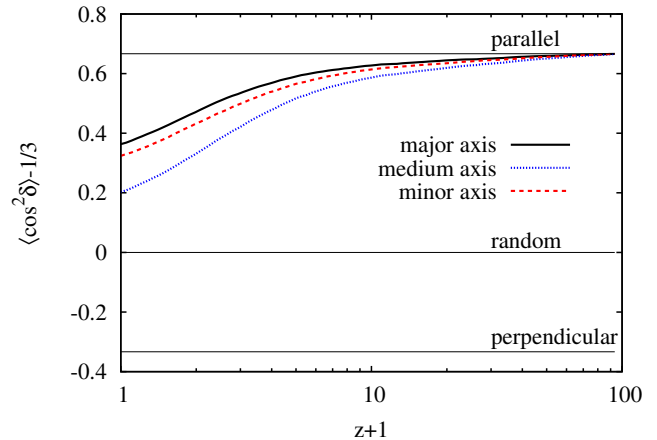


Figure 11. Orientation of void principle axes as a function of redshift. The orientation is measured by the angle δ spanned by the principle axes from initial conditions to redshift z . Parallel configuration (no evolution of void orientations) corresponds to $2/3$, whereas random configuration (evolution entirely erasing initial orientations) to 0. The orientations of void principle axes at late time retain a large part of the initial configuration.

the primordial density field of initial conditions and to what degree it is modified in a phase of non-linear evolution of structure formation.

We measure relative orientations of voids as the angle θ between the corresponding principle axes of voids in pairs. The principle axes are assumed to be eigenvectors of the shape tensor. We quantify degree of alignment by calculating $\langle \cos^2 \theta \rangle - 1/3$ which equals to $2/3$ for perfectly parallel orientations, 0 for random orientations and $-1/3$ for perfectly perpendicular orientations. We consider void pairs

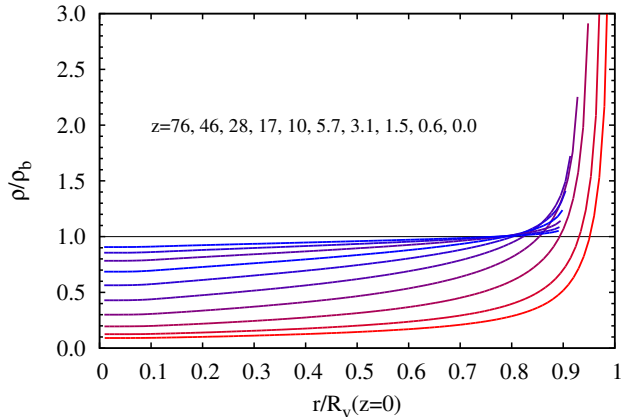


Figure 12. Redshift evolution of the mean matter density distribution inside voids. The profiles relate densities of isodensity surfaces to effective radii r of volumes enclosed by them. Using isodensity surfaces complies with the actual shapes of voids. The redshift sequence of the density distributions demonstrates formation of the final density profile with a characteristic bucket-like shape, i.e. nearly flat profile at $r \lesssim 0.9R_v$ and a sharp transition to the walls at $r \approx R_v$. The selected voids have effective radii $6h^{-1}\text{Mpc} < R_v < 20h^{-1}\text{Mpc}$ at $z = 0$.

with void separations less than $15h^{-1}\text{Mpc}$ at which voids are maximally aligned at redshift $z = 0$ (Platen et al. 2008). We use the same pairs of voids at all redshifts. In order to avoid potential biases due to hierarchical relations between voids, we discard all void-subvoid pairs.

Fig. 10 shows alignment of voids as a function of redshift. We find that voids at redshift $z = 0$ exhibit strong and comparable alignment in major and minor axes, but nearly random orientations in medium axes, in full agreement with Platen et al. (2008). Alignment of voids clearly undergoes some weak modifications in a phase of non-linear evolution. Compared to voids at $z = 0$, voids at high redshifts (including initial conditions) are slightly more aligned in major axes than in medium axes. These differences, however, are quite small compared to the initial alignment at $z = 100$. We therefore conclude that the current alignment of voids at $z = 0$ is in large part determined by the Gaussian primordial density field.

Fig. 11 reinforces our argument laid out above. It shows redshift evolution of void orientations measured by the angle δ spanned by the principle axes over time from initial conditions to redshift z . The evolution appears not to erase the initial orientations of void principle axes. The orientations of voids at late time retain a large part of the initial configuration acquired in the primordial density field. The correlation between the initial and final principle axes is far stronger than mutual alignments of void principle axes shown in Fig. 10.

4.4 Matter density distribution

Most studies on the matter density distribution in voids assume spherical symmetry (see e.g. Hamaus et al. 2014; Sutter et al. 2014b,c). This approach is well justified when considering composite voids made by stacking individual ob-

jects together. On the other hand, averaging in spherical shells seems to be inappropriate for measuring matter density distribution in individual voids due to a high degree of asphericity. Capturing the true physical matter distribution requires using geometry which is consistent with the actual shapes of voids, e.g. aspherical surfaces whose points are at equal distances from the void boundary. As shown by Cautun et al. (2016) and Cautun et al. (2015), this approach changes dramatically the picture conveyed by the spherical density profiles. The new matter density profiles have far more extended flat parts in void cores and exhibit a sharp transition to high density walls on void boundaries. Interestingly, these features are fully consistent with simple analytic models describing formation of spherical and isolated voids (see e.g. Sheth & van de Weygaert 2004).

Evolution of the matter density distribution in voids is driven in large part by matter evacuation in their cores and piling up matter on their boundaries. Capturing how both processes develop relies on computing matter density distribution in a way which complies with actual shapes of voids. Here we adopt the following approach. We sort all pixels inside a given void according to their densities. Then we construct a density profile by finding effective radius r of the volume given by all pixels with densities smaller than density $\rho(r)$. The resulting profile approximates closely a relation between densities of isodensity surfaces and effective radii of volumes enclosed by them. The choice of isodensity surfaces is a reasonable alternative to aspherical shells defined by equal distances from the void boundary (Cautun et al. 2016). As we shall see, both approaches give consistent results in terms of averaged density profiles.

Fig. 12 shows the evolution of the mean density profile. The redshift sequence of the profiles demonstrates clearly two main processes shaping the final density distribution in $z = 0$ voids: evacuation of matter in cores and formation of walls on the boundaries. The profiles of voids at highest redshifts evolve linearly with a symmetric growth of underdense and overdense parts. Intermediate redshifts show a transition to non-linear regime which breaks the symmetry between evolution of cores and walls. The final voids at redshift $z = 0$ develop eventually the density profiles with a characteristic bucket-like shape: wide cores and a sharp transition to high-density walls. These profiles resemble remarkably well analytic models describing evolution of a spherical and isolated void (see Sheth & van de Weygaert 2004). This resemblance is another justification that density profiles computed in a way which is consistent with the actual shapes of voids capture more physical properties than spherical density profiles.

The density profiles at low redshifts demonstrate effect of void expansion already shown in Fig. 6. Since evolution of void sizes can substantially differ between individual objects, it is instructive to split the void sample according to their expansion histories. Fig. 13 shows evolution of the mean density profiles in two extreme groups of voids: 10 per cent of most expanding and 10 per cent of most contracting voids (see the tails of the distribution in Fig. 7). The figure clearly demonstrates that expansion or contraction of void boundaries is independent of how the core evolves. It is directly related to how massive walls are developed around voids: voids with massive walls can undergo contraction, whereas voids with weak walls tend to expand. It is therefore not

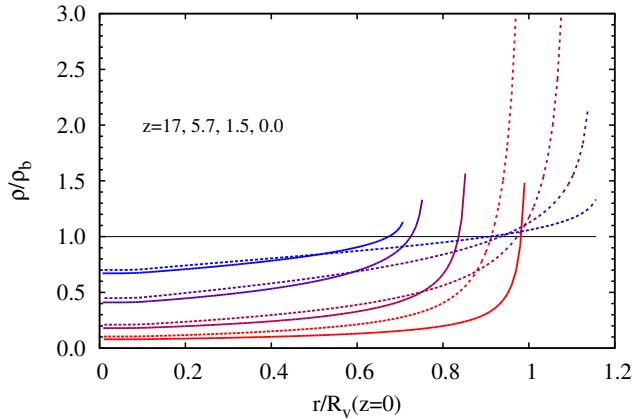


Figure 13. Redshift evolution of the mean density distribution inside 10 per cent of most expanding voids (solid lines) and 10 per cent of most contracting voids (dashed lines). The profiles relate densities of isodensity surfaces to effective radii r of volumes enclosed by them. Using isodensity surfaces complies with the actual shapes of voids and their progenitors. Despite distinct evolutions of the boundaries around the two types of voids, the cores undergo similar processes of matter evacuation. The expanding voids develop thinner walls, more extended cores part and a sharper transition between the core and the boundary walls. The selected voids have effective radii $6h^{-1}\text{Mpc} < R_v < 20h^{-1}\text{Mpc}$ at $z = 0$.

surprising that this relation reflects also levels of the void hierarchy. Subvoids develop weaker walls and their boundaries are dragged by super-Hubble flow of their host voids. On the other hand, voids at the top level of the hierarchy pile up massive walls which can likely start to collapse and shrink void interiors.

The two groups of most expanding and most contracting voids develop slightly different density profiles. The expanding voids (bottom levels in the void hierarchy) are characterized by larger cores, weaker walls and a sharper transition between the core and the boundaries. On the other hand, the contracting voids (top levels in the void hierarchy) develop more massive and thicker walls with a smoother transition between the core and the boundaries.

5 SUMMARY AND CONCLUSIONS

We have analysed performance of two different methods of tracking voids in cosmological simulations. The first approach is based on a direct application of a halo merger tree generator to void catalogues. Void tracking is performed by means of matching voids between successive snapshots of the simulation. The second approach has been developed for the purpose of this work and it finds voids in every snapshot of the simulation by tracking watershed basins of well formed voids. While the former method involves generating void catalogue at all snapshot, the latter builds the void catalogue only once.

We have shown that the method based on matching voids between successive snapshots gives rise to spurious instantaneous reconfigurations of voids. These effects are not physical and they are related to persistent reordering of minima and saddle points in the simulated density field,

in large part due to unresolved small-scale modes. We have demonstrated that the new method introduced in this work eliminates these problems and yields a continuous mapping between boundaries of voids at all redshift, from initial conditions to the present time.

We have applied the developed method of void tracking to cosmological simulations of a standard ΛCDM model. This has allowed us to study for the first time the redshift evolution of various properties of individual voids. We have restricted our studies to voids with effective radii between $6h^{-1}\text{Mpc}$ and $20h^{-1}\text{Mpc}$ at redshift $z = 0$. Our results can be summarized as follows.

- i. Initial void boundaries undergo complicated distortions caused by tidal forces acting in a late-time phase of the evolution. The spatial scale of these deformations is comparable to void sizes.
- ii. Evolution of void volumes is far less prominent than the boundary surfaces. On average voids increase their volumes by only 15 per cent. Individual voids can either expand or contract (collapse) depending on their location in the void hierarchy: expanding voids lie at the bottom of the hierarchy (subvoids), whereas collapsing voids at the top of the hierarchy. This connection is an additional factor modulating a well-known relationship between expansion rate of voids and their sizes (large voids tend to expand and small voids tend to contract or collapse).
- iii. Individual voids change their initial shapes acquired in the primordial density field. Evolution of void shapes proceeds in a way which barely modifies the overall distribution of axis ratios. This happens due to the fact that most elongated voids tend to become more spherical and the most spherical ones develop more elongated shapes. There is a weak trend of the major-to-minor axis ratio to decrease in time (developing gradually more elongated shapes of voids).
- iv. Evolution of voids does not erase their initial orientations. The orientations of void principle axes at late time are highly correlated with the initial ones.
- v. Major and minor axes of voids tend to be aligned at all redshifts. Lack of significant evolution suggests that void alignment origins in large part from the Gaussian primordial density field.
- vi. The new method of tracking voids in cosmological simulations allows us to capture redshift evolution of the matter density distribution in every individual void. Evolution of the matter density profiles in voids, computed on isodensity surfaces shows the formation of theoretically predicted profiles with a characteristic bucket-like shape indicating a vast core of nearly constant density and a sharp transition to high-density walls.
- vii. The matter evacuation in void cores is decoupled from the evolution of void boundaries. Evolution of void cores proceeds in the same way both in expanding and contracting voids. Unlike voids with boundaries dragged by super-Hubble flow, voids undergoing contraction tend to pile up thicker walls around them and a slightly smoother transition between the core and void boundary.

Despite clearly apparent evolution of every individual void, we conclude that the final voids do not substantially differ from their initial state in many respects. Apart from obvious difference in terms of the core density, voids retain a large part of properties acquired in the primordial den-

sity field such as shapes and orientations. It is even more surprising to notice that evolutionary paths of individual voids conspire to conceal any signature of evolution in overall statistics of voids. In particular, the evolution of axial ratios quantifying void shapes barely modifies the overall distribution over time. This reinforces the argument that tracing the evolution of individual voids in cosmological simulations unveils far more detailed aspects of void evolution than what one can learn from measuring overall distributions of various void properties in a range of redshifts.

ACKNOWLEDGEMENTS

RW would like to thank Rien van de Weygaert for useful discussions, Marius Cautun for critical reading of the manuscript and Ralf Kaehler for his help on 3D data visualization. The authors gratefully acknowledge the anonymous referee for constructive comments. RW acknowledges support through the Porat Postdoctoral Fellowship. The Dark Cosmology Centre is funded by the Danish National Research Foundation.

REFERENCES

- Abel T., Hahn O., Kaehler R., 2012, *MNRAS*, 427, 61
- Angulo R. E., Chen R., Hilbert S., Abel T., 2014, *MNRAS*, 444, 2925
- Aragon-Calvo M. A., Szalay A. S., 2013, *MNRAS*, 428, 3409
- Aragon-Calvo M. A., van de Weygaert R., Araya-Melo P. A., Platen E., Szalay A. S., 2010, *MNRAS*, 404, L89
- Bond J. R., Kofman L., Pogosyan D., 1996, *Nature*, 380, 603
- Bos E. G. P., van de Weygaert R., Dolag K., Pettorino V., 2012, *MNRAS*, 426, 440
- Cai Y.-C., Padilla N., Li B., 2015, *MNRAS*, 451, 1036
- Cautun M., Cai Y.-C., Frenk C. S., 2016, *MNRAS*, 457, 2540
- Cautun M., van de Weygaert R., Jones B. J. T., 2013, *MNRAS*, 429, 1286
- Cautun M., van de Weygaert R., Jones B. J. T., Frenk C. S., 2014, *MNRAS*, 441, 2923
- Cautun M., van de Weygaert R., Jones B. J. T., Frenk C. S., 2015, *ArXiv e-prints* 1501.01306
- Colberg J. M. et al., 2008, *MNRAS*, 387, 933
- Desjacques V., Smith R. E., 2008, *Phys. Rev. D*, 78, 023527
- Eisenstein D. J., Hu W., 1998, *ApJ*, 496, 605
- Falck B., Neyrinck M. C., 2015, *MNRAS*, 450, 3239
- Gottlöber S., Lokas E. L., Klypin A., Hoffman Y., 2003, *MNRAS*, 344, 715
- Hahn O., Abel T., 2011, *MNRAS*, 415, 2101
- Hahn O., Abel T., Kaehler R., 2013, *MNRAS*, 434, 1171
- Hahn O., Angulo R. E., 2016, *MNRAS*, 455, 1115
- Hahn O., Angulo R. E., Abel T., 2015, *MNRAS*, 454, 3920
- Hahn O., Porciani C., Carollo C. M., Dekel A., 2007, *MNRAS*, 375, 489
- Hamaus N., Sutter P. M., Wandelt B. D., 2014, *Physical Review Letters*, 112, 251302
- Hellwing W. A., Juszkiewicz R., 2009, *Phys. Rev. D*, 80, 083522
- Hockney R. W., Eastwood J. W., 1988, *Computer Simulation Using Particles*. Taylor & Francis, Inc., Bristol, PA, USA
- Hoffman Y., Metuki O., Yepes G., Gottlöber S., Forero-Romero J. E., Libeskind N. I., Knebe A., 2012, *MNRAS*, 425, 2049
- Icke V., 1984, *MNRAS*, 206, 1P
- Kaehler R., Hahn O., Abel T., 2012, *IEEE Transactions on Visualization and Computer Graphics*, 18, 2078
- Lambas D. G., Lares M., Ceccarelli L., Ruiz A. N., Paz D. J., Maldonado V. E., Luparello H. E., 2016, *MNRAS*, 455, L99
- Lavaux G., Wandelt B. D., 2012, *ApJ*, 754, 109
- Lee J., Jing Y. P., Suto Y., 2005, *ApJ*, 632, 706
- Li B., Zhao G.-B., Koyama K., 2012, *MNRAS*, 421, 3481
- Neyrinck M. C., 2008, *MNRAS*, 386, 2101
- Paz D., Lares M., Ceccarelli L., Padilla N., Lambas D. G., 2013, *MNRAS*, 436, 3480
- Planck Collaboration et al., 2014, *A&A*, 571, A16
- Platen E., van de Weygaert R., Jones B. J. T., 2007, *MNRAS*, 380, 551
- Platen E., van de Weygaert R., Jones B. J. T., 2008, *MNRAS*, 387, 128
- Powell D., Abel T., 2015, *Journal of Computational Physics*, 297, 340
- Sahni V., Sathyaprakah B. S., Shandarin S. F., 1994, *ApJ*, 431, 20
- Shandarin S., Feldman H. A., Heitmann K., Habib S., 2006, *MNRAS*, 367, 1629
- Shandarin S., Habib S., Heitmann K., 2012, *Phys. Rev. D*, 85, 083005
- Sheth R. K., van de Weygaert R., 2004, *MNRAS*, 350, 517
- Sousbie T., Colombi S., 2015, *ArXiv e-prints* 1509.07720
- Springel V., 2005, *MNRAS*, 364, 1105
- Sutter P. M., Elahi P., Falck B., Onions J., Hamaus N., Knebe A., Srisawat C., Schneider A., 2014a, *MNRAS*, 445, 1235
- Sutter P. M. et al., 2015, *Astronomy and Computing*, 9, 1
- Sutter P. M., Lavaux G., Hamaus N., Wandelt B. D., Weinberg D. H., Warren M. S., 2014b, *MNRAS*, 442, 462
- Sutter P. M., Lavaux G., Wandelt B. D., Weinberg D. H., Warren M. S., 2014c, *MNRAS*, 438, 3177
- van de Weygaert R., Platen E., 2011, *International Journal of Modern Physics Conference Series*, 1, 41
- van de Weygaert R., van Kampen E., 1993, *MNRAS*, 263, 481
- Way M. J., Gazis P. R., Scargle J. D., 2015, *ApJ*, 799, 95
- Yang L. F., Neyrinck M. C., Aragón-Calvo M. A., Falck B., Silk J., 2015, *MNRAS*, 451, 3606